Fe₃C decorated wood-derived integral N-doped C cathode for rechargeable Li-O₂ batteries

Huagen Liang [a], Zejia Gai [b], Fu Chen [a,d], Shengyu Jing [b,*], Wei Kan [c], Bing Zhao [c,*], Shibin Yin [e], Panagiotis Tsiakaras [f,*]

[a] Carbon Neutrality Institute, School of Materials Science and Physics, China University of Mining and Technology, Xuzhou 221008, China
[b] School of Information and Control Engineering, China University of Mining and Technology, Xuzhou, Jiangsu 221008, China
[c] Heilongjiang Provincial Key Laboratory of Surface Active Agent and Auxiliary, Qiqihar University, Qiqihar 161006, China
[d] School of Public Administration, Hohai University, Nanjing 210098, China
[e] MOE Key Laboratory of new Processing Technology for Non-ferrous Metals and Materials, Guangxi Key Laboratory of Processing for non-ferrous Metals and Featured Materials, Guangxi University, Nanning, China
[f] Laboratory of Alternative Energy Conversion Systems, Department of Mechanical Engineering, School of Engineering, University of Thessaly, Pedion Areos 38834, Greece

ARTICLE INFO

ABSTRACT

Herein, an integral Fe₃C decorated wood-derived Fe, N co-doped carbon (N-wdC-MS) was developed via one-step pyrolysis of $FeCl_3$/LiCl impregnated paulownia-wood and melamine, which can be directly used as Li-O₂ battery cathode. This three-dimensional (3D) free-standing cathode inherited the aligned channels of wood, ensuring unimpeded O₂/electrolyte supply. The etching effect of $FeCl_3$/LiCl mixed molten salt enlarges the porous-structure of carbonized-wood, expanding three-phase boundary. Fe₃C@NC aggregates evenly grew on the surface and channels of carbonized wood, which act as catalytic sites. Moreover, in aqueous solution, N-wdC-MS showed excellent oxygen reduction reaction/oxygen evolution reaction catalytic activity. With these advantages, the Li-O₂ battery assembled with N-wdC-MS as cathode deliver a superhigh specific capacity of 50.28 mAh cm^{-2} at a current density of 0.1 mAcm^{-2}, and the cycle-life can maintain 190 times. This low-cost and easily available wood-based electrode provides a new idea for designing and large-scale production for cathode of other Metal-Air/Metal-S batteries.

1. Introduction

At present, the energy density of commercialized lithium-ion batteries is unable to meet long driving range requirements. Mileage anxiety is the main obstacle for the popularity of Lithium-ion batteries-powered electric vehicles [1]. Among many new secondary batteries, Li-O₂ batteries have attracted extensive attention, due to their advantages of ultra-high energy density and environmental friendliness [2–4]. However, the problems of poor rate performance, short cycle life and high discharge/charge overpotential still hinder their commercialization [5–7]. The main reason for the above problems is the sluggish kinetics of oxygen reduction reaction (ORR) and oxygen evolution reaction (OER) occurred at cathode. In addition, the insulating and insoluble discharge products, generated in cathode, block the diffusion channels of O₂ and Li$^+$ and isolate the catalytic active sites, so as to terminate the reaction. To overcome these challenges, it is necessary to fabricate cathodes with high catalytic activity and efficient mass transfer [8–10].

So far, researchers have made great efforts to develop advanced ORR/OER bifunctional catalysts and improve the structure of cathodes [11,12]. The conclusion was that the ideal cathode must have good conductivity and possess relatively open channels to ensure smooth O₂ and electrolyte supply. Secondly, microporous-mesoporous hierarchically pore structure is indispensable to expose more active sites. More importantly, efficient ORR/OER catalytic activity is the primary factor in reducing discharge/charge overpotential. Additionally, avoiding binder in the manufacturing of cathode not only reduces the occurrence of side reactions but also simplifies the production procedure.

Among the multiple candidates, biomass was regarded as a class of perfect raw materials for the preparation of self-standing electrodes, which possess a natural 3D structure and could be converted to carbon

---

* Corresponding authors.
E-mail addresses: jingshengyu@126.com (S. Jing), zhao_submit@aliyun.com (B. Zhao), tsiak@uth.gr (P. Tsiakaras).

skeleton with good electronic conductivity [13–15]. In addition, biochar-derived flexible materials have more competitive advantages in terms of price than commercial carbon paper, carbon cloth, or metal foam, and were widely used as electrode components for water splitting [16], batteries [17], supercapacitors [18], and so on [19,20]. Hu's group [21–25] has made some fruitful attempts to prepare a sequence of 3D self-standing wood-based cathodes for Li-O$_2$/Li-CO$_2$ batteries by delignification-carbonization and loading with Ru/RuO$_2$ nanocatalysts. The vertically arranged channels of wood can be easily infiltrated by electrolyte to form a transmission highway of O$_2$ and Li$^+$. The micropores on the wall of channels can anchor Ru/RuO$_2$ nanoparticles to form countless catalytic reaction zones. For example, CA-wood-Ru cathode showed a good specific area capacity of 8.58 mAh cm^{-2} in Li-O$_2$ battery. The capacity further increased to 56.0 mA h cm^{-2} when the thickness of CA-wood-Ru increased to 3.4 mm, due to the enhanced accommodation space for discharge products.

Although the catalytic activity of noble metals (Pt, Ru, RuO$_2$, and so on) are dazzling, rareness makes them difficult for large-scale application. In order to prepare N-doped self-standing carbonized wood electrode (wd-NC), Luo et al. [26] calcined yellow pine in NH$_3$ atmosphere. N-doping effectively enhanced the catalytic role of carbonized wood, resulting in an improvement of the specific capacity and cycle performance of Li-O$_2$ batteries with wd-NC, as compared to the one with wd-C. Tang et al. [27] used basswood as raw material and trisulfide cyanamide as N and S sources to obtain N, S co-doped carbonized wood through carbonization and NH$_3$ activation. They found that the ORR performance of N, S co-doped carbonized wood is comparable to that of commercial Pt/C catalyst in an alkaline medium. Peng et al. [28] prepared N-doped carbonized wood with high-density graded pore structure by enzyme solution pretreatment and pyrolyzation with NH$_4$Cl, which showed good ORR/OER activity. The authors suggested that the enzyme solution could hydrolyze and digest the cellulose in wood and generate a large number of nanopores on the wall of channels, resulting in enhancement of the defect degree of carbonized wood. Moreover, graphite-N and pyridine-N were introduced into the carbon skeleton from the decomposition of NH$_4$Cl, which promoted the ORR/OER activity of carbonized wood. Melamine, as an organic compound with the highest nitrogen content, is usually used as the raw material for the preparation of N-doped carbon materials [29,30]. In addition, melamine is a cheap N precursor, and it is easy to store. Compared with other N-doping ways, the process of preparing N-doped carbon by calcination of the mixture of melamine and carbon precursor is very simple. Meanwhile, the N-doping amount can be easily controlled by the dosage of melamine. However, the catalytic activity of doped carbon is a frustrating contrast to metal-based catalysts. FeCo@NS-CA aerogel was prepared by the carbonization of the mixture of lignin removed light-wood and dicyandiamide, thiourea, FeCl$_3$, and Co(NO$_3$)$_2$ [31]. Compared with NS-CA aerogel only doped with N and S, the ORR/OER activity of FeCo@NS-CA aerogel increased significantly. The strong metal-matrix interaction between FeCo alloy and doped carbon matrix is the source for improving the performance. Cui et al. [32] prepared an integral Co/CoO@NWC electrode by using N-doped carbonized wood as support and by loading Co(OH)$_2$ via electrodeposition and thermal activation in Ar atmosphere. The ORR and OER activities of Co/CoO@NWC were close to the commercial 20 % Pt/C and RuO$_2$, which were much higher than that of NWC. The above studies show that N-doped biochar loading with high activity catalyst may be a good strategy to reduce the ORR/OER overpotentials and avoid the corrosion of carbon, especially for the Li-O$_2$ batteries. However, most of these methods are complex, time-consuming, and laborious, which need to be further improved. Ion thermal technology with molten salt as a medium is a simple process for the synthesis of high porosity carbon materials [33,34]. This technology does not involve the use of hazardous substances and high pressure, which is environmentally friendly and easily scalable.

In this work, a novel integral Fe$_3$C decorated wood-derived N-doped

C (N-wdC-MS) was prepared by calcination of LiCl/FeCl$_3$ impregnated paulownia and melamine, which was directly employed as the cathode for Li-O$_2$ battery. The mixed molten salt of FeCl$_3$ and LiCl with a molar ratio of 1:1 has a low co-melting point, which acts as an etchant at high temperature and creates more pores for carbonized wood. Melamine is regarded as a carbon source containing heteroatoms, which introduced N dopant into the carbon skeleton under the catalysis of Fe. Consequently, the Li-O$_2$ battery with N-wdC-MS exhibited superior electrochemical performance and cycle stability. This simple one-step method provides a feasible strategy for large-scale production of cheap and efficient cathodes for Li-O$_2$ batteries.

2. Experimental

2.1. Fabrication of wood derived cathode

Firstly, paulownia wood was sliced up into round flakes (thickness≈1.5 mm, diameter≈10 mm) perpendicular to the growth direction and then cleaned with distilled water and anhydrous ethanol. Then, the dry and clean wood slices were soaked in 20 mL of FeCl$_3$/LiCl (molar ratio 1:1) ethanol solution with a concentration of 5 M. After stirring at 60 °C for 24 h, the wood slices fully adsorbed FeCl$_3$/LiCl were taken out and dried in a vacuum oven for standby. Melamine (2 g) and the dried wood slices loaded with FeCl$_3$/LiCl were put in two porcelain boats and placed at upstream and downstream in the tubular furnace, respectively. After carbonization at 900 °C for 1 h in Ar atmosphere, the obtained products were treated by 1 M HNO$_3$ etching for 24 h, and then washed with distilled water and ethanol 3 times, named as N-wdC-MS. wdC was prepared by directly carbonization of round wood flakes in the same way. N-wdC was prepared by carbonization of round wood flakes and melamine in the same way. The wdC-MS sample was prepared by direct carbonization of FeCl$_3$/LiCl impregnated round wood flakes in the same way.

2.2. Characterization and measurements

Scanning electron microscopy (SEM, Hitachi S4800) was employed to investigate the morphology of the as-prepared samples and transmission electron microscopy (TEM, FEI Tecnai-20) was used to observe their detailed structure. X-ray diffraction (XRD, Bruker D8-Advance) was applied to characterize the phase formation. The surface composition and chemical state were studied by X-ray photoelectron spectroscopy (XPS, ESCALAB 250Xi). The specific surface area and pore structure were measured by N$_2$ isothermal adsorption and desorption (Quantachrome Autosorb iQ Station 2). The defect degree of carbon in each sample was tested by a laser Raman spectrometer (Bruker Senterra, $\lambda = 532$ nm).

2.3. Electrocatalytic activity evaluation and Li-O$_2$ Battery test

The *off-line* ORR/OER activity of the as-prepared samples was performed on a CHI 760D electrochemical workstation with a three-electrode system. A graphite rod and a saturated calomel electrode were used as the counter and reference electrode, respectively. Before the electrode preparation, the as-prepared samples are first ground into powder. The catalyst slurry was prepared by mixing the powder sample (2 mg), ethanol (0.8 mL), and 5 wt % Nafion solution (0.2 mL). 15 μL slurry was dropped carefully onto the rotating-disk electrode (RDE). The working area of RDE is 0.196 cm^2. Before the ORR/OER test, the electrolyte (0.1 M KOH solution) was bubbled with Ar or O$_2$ for 30 min *In-situ* cyclic voltammetry (CV) and electrochemical impedance spectroscopy (EIS) were performed on an electrochemical workstation (Princeton PARSTAT 4000, USA) in a two-electrode mode. The cathode was recognized as the working electrode, while Li foil was recognized as the reference and counter electrode. The voltage range of in-situ CV experiments was 2.0–4.5 V and the scan rate is 0.1 mV s^{-1}. EIS of Li-O$_2$

battery at different states (initial state, 1st discharge ending state, and 1st charge ending state) was measured under open-circuit condition. The frequency range of EIS measurement is 100 kHz to 10 mHz and the Ac voltage amplitude of 5 mV.

A CR 2025-type coin cell with $17 \times \Phi 1.0$ mm holes on the positive shell was used to evaluate the performance of Li-O$_2$ batteries. Each button cell consists of a glass fiber (Whatman GF/D) separator, Li foil, and a piece of the as-prepared cathode. 1 M LiTFSI/TEGDME was used as the electrolyte and the amount of electrolyte in each cell was 100 μL. All the cells were assembled in the glove box filled with Ar (MBRAUN, H$_2$O&O$_2$ <0.5 ppm). The assembled coin cell was transferred to a sealed glass bottle and filled with 1 atm pure O$_2$. The rate and cycle performance of Li-O$_2$ battery was tested on Neware battery testing instrument (CT-3008, China) between 2.0 and 4.5 V (vs Li/Li$^+$). Before the test, the batteries rested for 5 h. The specific capacities are normalized by the geometric area of cathode.

3. Results and discussion

3.1. Physicochemical characterization

The fabrication of 3D self-standing N-wdC-MS cathode involves two steps: impregnation and carbonization (show as Fig. 1). Firstly, the wood slices were soaked in the ethanol solution of FeCl$_3$/LiCl and dried to obtain the precursor. Second, the melamine and the precursor were placed at the upstream and downstream of tubular furnace, respectively. After calcination at 900 °C, N-wdC-MS was obtained. According to the literature [32], 900 °C can ensure the complete carbonization of wood. The co-melting point of FeCl$_3$/LiCl mixed salt with molar ratio of 1:1 is only 150 °C (http://www.factsage.cn/fact/documentation/FTsalt/FeCl$_3$-LiCl.jpg), which can be melted to nanodroplets at high temperature and penetrate into the wood. Melamine offers N atoms for doping and increase the hydrophilicity of the electrode surface [35, 36].

To understand the phase composition of as-prepared samples, XRD tests were carried out, and the results are shown in Fig. 2a and S1. As can be seen from Fig. 2a, there is a significant diffraction peak at ~26°, which can correspond to the (002) plane of graphite carbon, indicating that the carbon in N-wdC-MS presents a good crystallinity. In addition, the diffraction peaks at 42.8°, 44.9° and 54.4° could be attributed to the (211), (031) and (230) crystal planes of Fe$_3$C (JCPDF: #65–2413), respectively, indicating the existence of Fe$_3$C in the sample. Therefore, it can be considered that N-wdC-MS is composed of Fe$_3$C and graphite carbon. According to previous studies, the presence of Fe$_3$C may have a positive effect on the ORR/OER catalytic activity of the composites [37–39] and carbon with high graphitization degree is conducive to the rapid conduction of electrons.

It can be seen from Fig. S1 that the wdC obtained by direct calcination has less obvious graphite carbon diffraction peaks. Biochar generally belongs to hard carbon, meaning that biomass is difficult to graphitize and the graphitization temperature exceeds 2500 °C. When melamine was added to the reaction system, the peak intensity of the diffraction peak at 26° increased significantly. Because melamine is a six membered cyclic molecular compound composed of C, N and H atoms, it is easy to form a six-membered graphite ring by high temperature carbonization. It is noteworthy that the characteristic peak of graphite of wdC-MS and N-wdC-MS becomes much stronger compared with those of wdC and N-wdC, due to the introduction of FeCl$_3$/LiCl. This phenomenon can also be found in previously published investigations [40]. Liu et al. [41] found that the graphitization degree (the peak intensities of (002) plane) of glucose derived carbon was significantly enhanced in the presence of FeCl$_2$. They considered that Fe is the most active catalyst for graphitization, whatever in the oxidation state or other chemical form [42]. In this work, FeCl$_3$/LiCl mixed salt melted and formed nanodroplets, which penetrated into wood and catalyze to form carbon skeleton with high graphitization degree [43].

Fig. 2b shows the pore structure of N-wdC-MS. According to International Union of Pure and Applied Chemistry (IUPAC) classification, N-wdC-MS showed typical type IV adsorption isotherms and type IV hysteresis loops. According to the multipoint Brunauer-Emmett-Teller theory, it is calculated that the total specific surface area is 295.31 m^2 g^{-1}, and the pore volume of N-wdC-MS is 0.41 cm^3 g^{-1}.

Fig. S2 displays a comparison between N$_2$ adsorption-desorption isotherms of several cathodes. Firstly, it can be seen from the ordinate of Fig. S2a that the adsorption capacity of wdC can reach ~300 cm^3 g^{-1}, which sharply drops to ~30 cm^3 g^{-1} after the addition of melamine (N-wdC). When only FeCl$_3$/LiCl molten salt is introduced into the reaction system, the adsorption capacity of wdC-MS increases to ~600 cm^3 g^{-1}. Further, after introducing at the same time melamine and FeCl$_3$/LiCl molten salt into the reaction system, the adsorption capacity (~300 cm^3 g^{-1}) is smaller than wdC-MS, but much higher than that of N-wdC. The above results show that wdC prepared by the directly pyrolyzed possesses abundant pores, which will be conducive to the efficient diffusion of O$_2$ in the electrode. The products of melamine pyrolysis may block the pores in wood, resulting in lower porosity and less adsorption of N$_2$ molecules. FeCl$_3$/LiCl molten salt may play the role of etching [44,45] or intercalation [42,46], which could generate more holes on the surface and inside of wood at 900 °C.

From the analysis of N$_2$ adsorption-desorption isotherms, we found that the adsorption capacity of wdC, wdC-MS and N-wdC-MS showed a rapid upward trend in the region of low relative pressures ($P/P_0 \approx 0$), indicating that in the material there is a large number of micropores [47]. However, the adsorption capacity of N-wdC hardly changes under the same relative pressure, which may be related to the micropores in
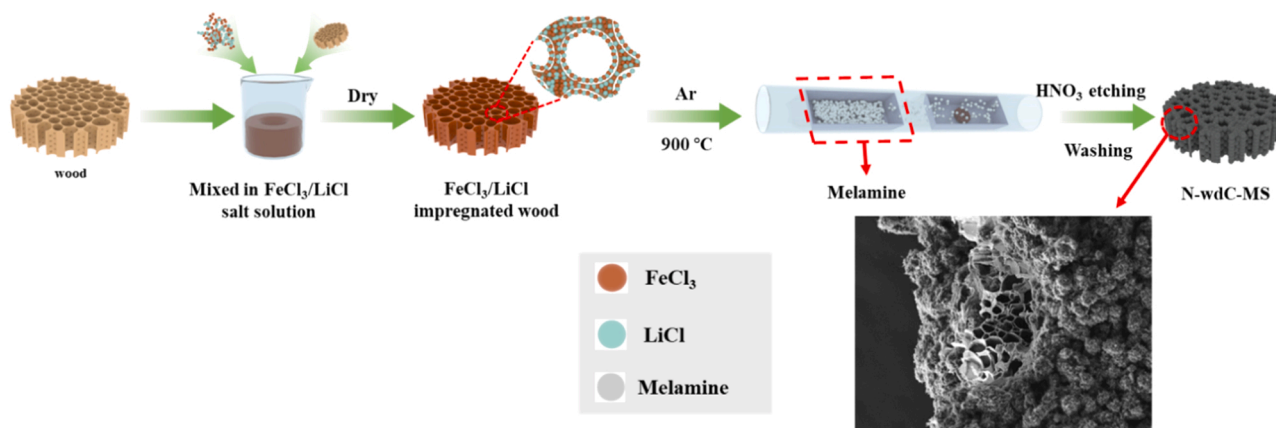

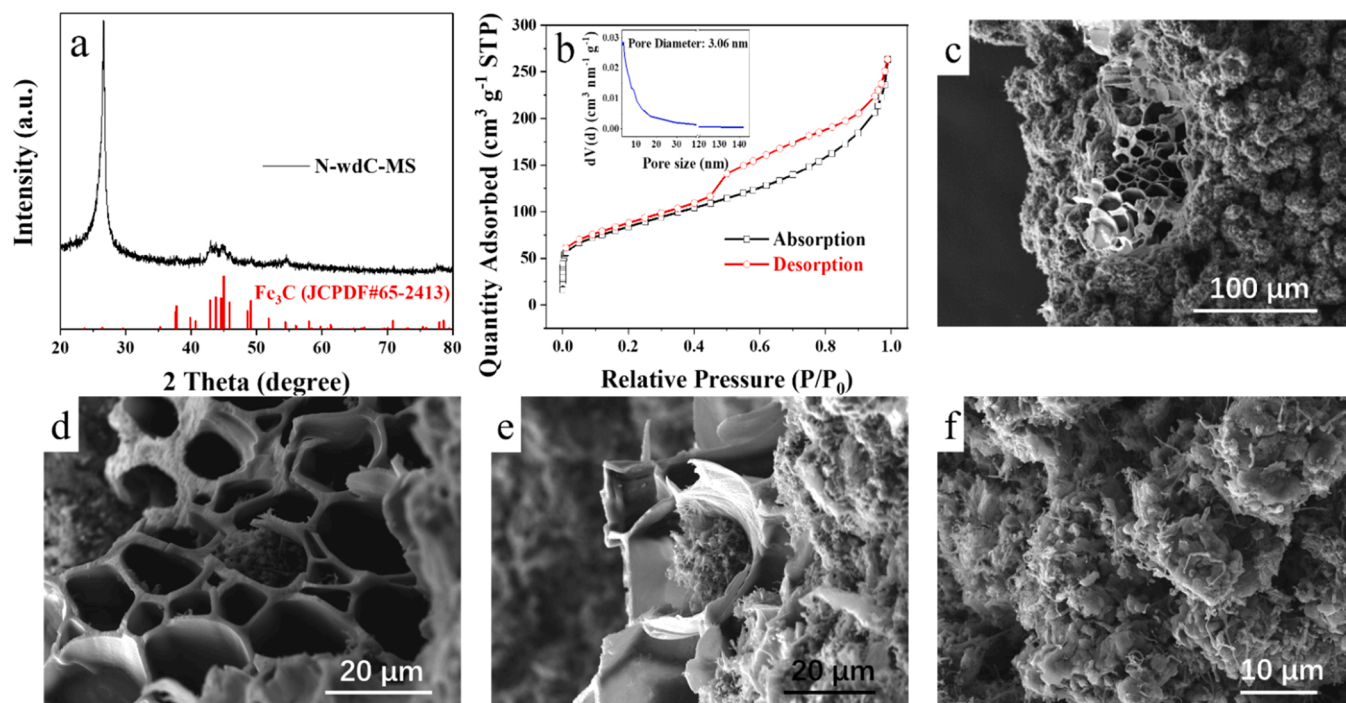**Fig. 1.** Schematic diagram for the preparation of N-wdC-MS.

Fig. 2. XRD patterns (a), N_2 adsorption-desorption isotherms and pore size distribution (b) and SEM images (c-f) of N-wdC-MS.

the carbonized wood filled by the melamine decomposition products. Secondly, it can also be observed that wdC and N-wdC show similar hysteresis loops in the range of 0–1.0 (P/P_0), indicating that they only have micropores and macropores. However, the hysteresis loops of wdC-MS and N-wdC-MS are quite different, appearing in the relative pressure region from 0.4 to 0.9. In addition, the non-coincidence degree of desorption line and adsorption line of N-wdC-MS is higher than wdC-MS, indicating that the mesopores proportion of N-wdC-MS is higher. According to IUPAC classification, wdC shows the typical type II isotherm and H3 hysteresis loop, N-wdC shows typical type III isotherm and H3 hysteresis loop, while wdC-MS shows the typical type IV isotherm and H4 hysteresis loop.

Figs. S2b & S2c show the microporous pore size distribution and the mesoporous pore size distribution of the four electrodes, calculated by Horvath-Kawazoe (HK) and Density Function Theory (DFT) method, respectively. As can be seen from Fig. S2b, N-wdC presents almost no microporosity compared with wdC, and the microporous volume of N-wdC-MS is significantly lower than that of wdC-MS, which is consistent with the above description of adsorption capacity. When $FeCl_3$/LiCl molten salt is introduced into the reaction system, the micropore volume ratio of wdC-MS is significantly improved. Furthermore, it can be found that the pore size of wdC-MS and N-wdC-MS slightly shift-right compared with that of wdC (~0.52 nm), which is mainly concentrated at ~0.55 nm. As illustrated in Fig. S2c, there is a large number of mesopores in wdC, and the pore size is mainly concentrated at 6.38 nm. Although the pore volume of N-wdC is decreased compared to wdC, the pore size is slightly increased, ascribed to the porous carbon layers formed by the pyrolysis of melamine formed on the carbonized wood. After the $FeCl_3$/LiCl molten salt addition, the pore size distribution of mesoporous become wider, which proves again that molten salt is favorable for manufacturing more pores and more catalytically active sites in the electrode materials. The introduction of melamine may produce various forms of N-doped carbon under the catalysis of Fe, which is also conducive to the improvement of catalytic activity. Table S1 lists the pore structure parameters of these four samples. It is obvious that the BET area follows the order of wdC < N-wdC < N-wdC-MS < wdC-MS and the average pore size follows the order of N-wdC

< wdC < N-wdC-MS < wdC-MS. It is worth mentioning that the mesoporous ratio of N-wdC-MS is the highest among several materials.

Fig. 2c-f show the morphology of N-wdC-MS. From the SEM images can be revealed the cellular pore characteristic of N-wdC-MS (the left side of Fig. 2c), inherited from the natural vertical channel of wood (as shown in Fig. S3c). On the right side of Fig. 2c, it can be seen that the surface is attached by a large number of loose particle aggregates similar to mulberry. From Fig. 2d & e, it can also be seen that these particle aggregates grow in the channel and on the inner wall of the carbonized wood. Further magnification, it can be found that they are composed of fibers and nanoparticles (Fig. 2d), which may be due to the generation of Fe_3C and N-doped carbon nanofibers from the reaction of melamine and $FeCl_3$. Figs. S3a-f compares the SEM images of several other samples. wdC shows a typical honeycomb channels characteristic (Fig. S3a), which is consistent with that reported in the literatures, but the wall looks smooth and dense (Fig. S3b). Macroscopically, N-wdC still maintains a honeycomb channel structure (Fig. S3c), but its surface appears thicker. Carbon layers seem to be deposited around the small holes on the inner wall (Fig. S3d), which may be the root cause of the significant decrease of BET area and pore volume for N-wdC. The wdC-MS also shows the channel structure (Fig. S3e), but massive aggregates grown on its surface (Fig. S3f), which may be that the volatile compounds of wood reacts with $FeCl_3$ to form Fe_3C during calcination.

Clearly, adding melamine or molten salt alone and adding melamine and molten salt at the same time, the final product shows contrasting morphology. We believe that: N-wdC-MS, on the one hand, inherits the vertical channel structure of wood, ensuring the rapid O_2 diffusion and electrolyte mass transfer [48,49]. On the other hand, the rich of micropores-mesopores structure also facilitates to amplify the three-phase reaction interface, and the Fe_3C and N-doped carbon fibers generated on the surface and pores exposed the catalytic active sites [50].

The high-resolution TEM images of N-wdC-MS indicate that Fe_3C aggregates composed of nanoparticles (circled by white circles) grow on fibrous carbon (circled by red ellipse) (Fig. 3a). The lattice spacing of 0.23 nm corresponds to the (210) crystal plane of Fe_3C (Fig. 3b). As shown in the bright field (Fig. 3c) and dark field TEM (Fig. 3d), Fe_3C
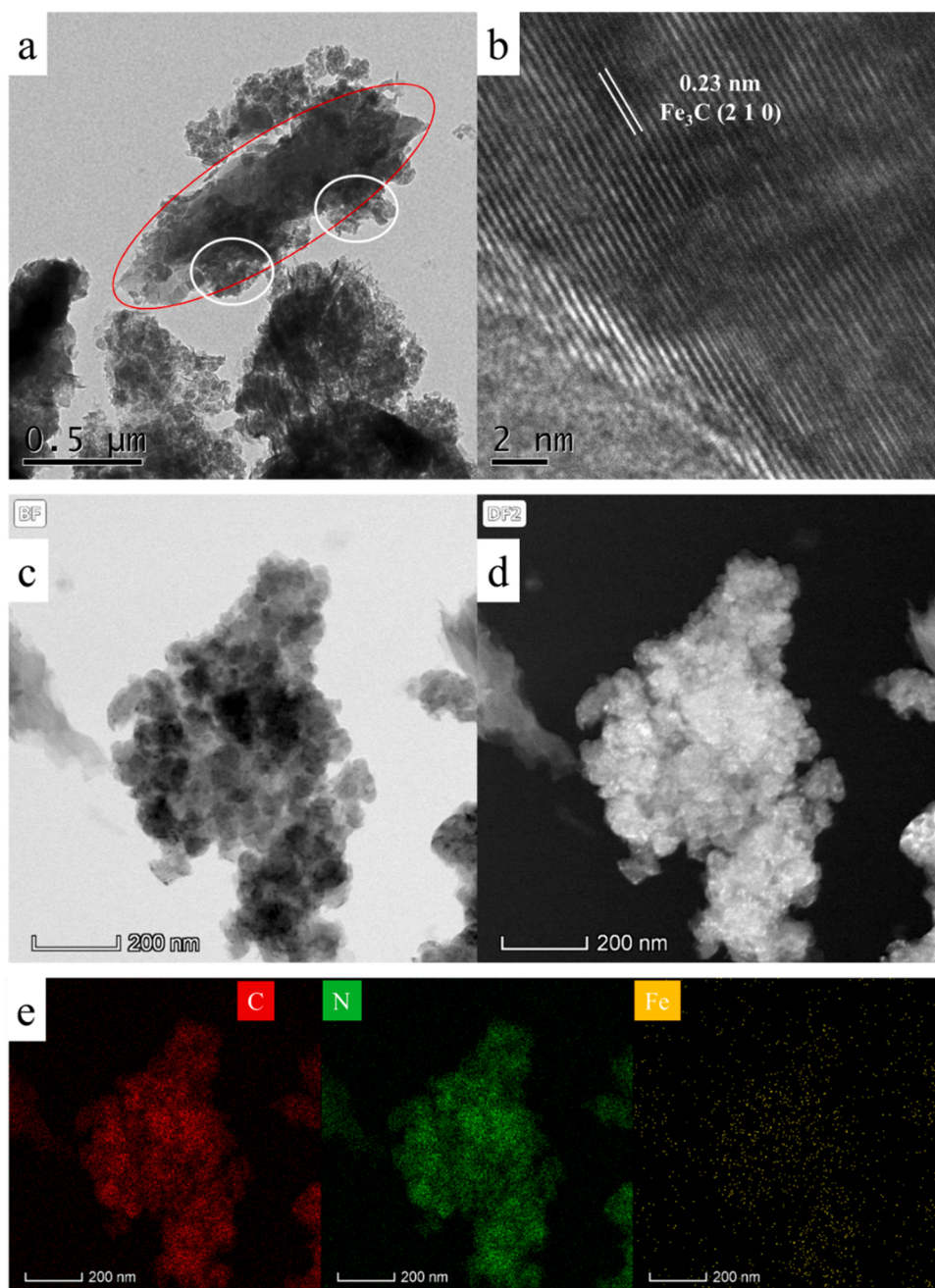
Fig. 3. TEM images of N-wdC-MS.

nanoparticles are evenly distributed and between these particles interstitial holes can be found. From the EDX (Energy Dispersive X-Ray Spectroscopy) elemental mapping images, it is clear that C, N and Fe are evenly distributed in the composite (Fig. 3e).

In order to study the defect information caused by melamine, Raman spectroscopy was carried out, as shown in Fig. 4a. In all samples, two well-defined peaks at 1354 and 1572 cm^{-1}, namely D band and G band, can be observed. It is well known that D band is produced by the hanging bond vibration of carbon atoms in the plane terminal, indicating the number and disorder degree of defects in carbon. G band corresponds to C-C bond of sp^2 hybridization with E2g symmetry vibration mode, which is related to the order of carbon and the degree of graphitization [51]. The intensities I_G/I_D ratio is used to measure the graphitization degree of carbon, so as to infer the electronic conductivity of carbon materials [52]. Clearly, the value of I_G/I_D of N-wdC-MS was higher than that of wdC, N-wdC and wdC-S, indicating that the higher graphitization

degree of carbon in N-wdC-MS, which is consistent with the results of XRD analysis. The good graphitization can ensure good electronic conductivity, and promote electron transmission in the cathode reaction process of Li-O$_2$ battery [37]. More importantly, a clear 2D band at ~2701 cm^{-1} can also be found in N-wdC-MS, which is regarded as the characteristic peak of graphene, attributing to the pyrolysis of melamine catalyzed by Fe. However, careful observation shows that the symmetry of the G band of N-wdC-MS is not perfect and seems to be composed of two peaks (Fig. S4). The Raman spectrum of N-wdC-MS can be fitted into five peaks, D$_1$, D$_2$, D$_3$, D$_4$ and G respectively. The D$_1$ peak represents a disordered structure caused by defects or heteroatoms with A1g symmetry; D$_3$ shows the C-C tensile-vibration, while D$_4$ signal provides information of the presence of polyene or ionic impurities; D$_2$ band is a shoulder of the G band, which also corresponds to a graphitic lattice mode with E2g symmetry. The defect degree of carbon material also can be evaluated by the ratio of I_{D1}/I_G [51,53]. The I_{D1}/I_G ratio of N-wdC-MS
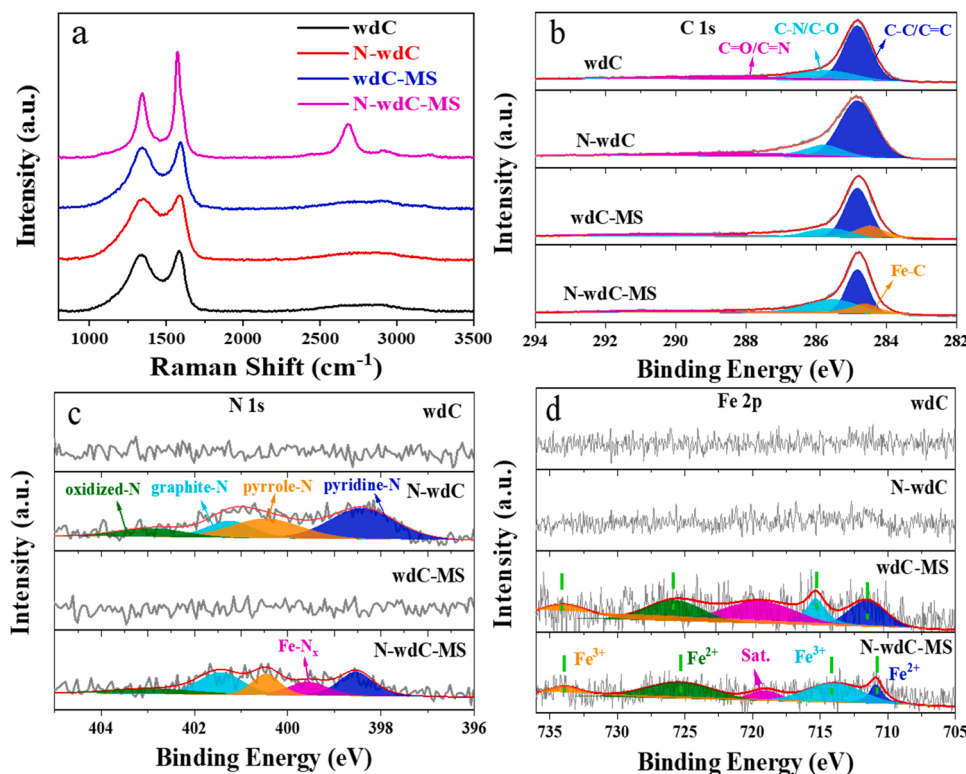
Fig. 4. Raman spectra (a) and high resolution C 1 s (b), N 1 s (c) and Fe 2p (d) XPS spectra of various cathodes.

is about 1.28, proving that there are many defects in the carbon component of N-wdC-MS. The defects may be originated from N-doping and the nanopores etched by $FeCl_3/LiCl$. These defects are helpful to promote ORR/OER catalytic activity.

Fig. 4b-d shows the XPS spectra of the four as-prepared samples. From the high-resolution C 1 s spectrum (Fig. 4b), it can be seen that the peaks at 284.8, 285.7 and 288 eV correspond to the C-C/C=C bonds, C-N/C-O bonds and C=N/C=O bonds, respectively. In particular, for wdC-MS and N-wdC-MS, the peak at 284.6 eV should be assigned to the Fe-C bond [54], indicating the formation of Fe_3C. The main component of wood is cellulose, and its protein content is low. It can be found that the N content of wdC and wdC-MS is 0. The detection of N element can be seen after introducing melamine. The N 1 s spectrum (Fig. 4c) can be simulated into four peaks of 398.3, 400.1, 401.2 and 402.5 eV, corresponding to pyridine-N, pyrrole-N, graphite-N and oxide-N respectively [55].

The N-wdC-MS sample contains a certain proportion of metal-N (399.1 eV). Pyridine-N occurs at the edge of the carbon material and was regarded as the electron donor to the π-bond, which is easier to approach the reactant (O_2) and electrolyte than the whole part. Pyrrolic-N is conducive to boost the OER onset potential [56]. Graphite-N and Metal-N are also acknowledged as the important catalytically active sites for ORR in acidic and alkaline aqueous solution [55,57]. As revealed in the high-resolution Fe 2p spectra of N-wdC-MS (Fig. 4d), two pairs of signals are identified as Fe $2p_{3/2}$ (710.8 and 725.3 eV) and Fe $2p_{1/2}$ (713.9 and 733.9 eV) with a satellite peak at 719.1 eV of Fe_3C as the main component of the Fe-C composite [50,58].

Transition metal carbides, such as Fe_3C, WC, and so on, possess "platinum-like" surface electronic structures and catalytic properties, which are reliable candidates for catalytic HER, ORR and OER [59,60]. To find out whether Fe_3C can be used as ORR catalytic active site, $M_3C@G$ (M: Fe, Co, Ni) was prepared via a hot filament chemical vapor deposition (HF-CVD) method, eliminating the influence of doping N elements [61]. Fe_3C, Co_3C and Ni_3C is considered as the only catalytic activity. Highly dispersed M_3C nanocrystals coupled with the surface

graphite layer are conducive to improving catalytic activity and stability. Zhu et al. [62] prepared a 3D self-standing Fe_3C/Ni-foam electrode by hydrothermal reaction and low temperature annealing treatment. The overpotentials of OER at 50 mA cm^{-2} and the Tafel slope of the as-prepared Fe_3C/Ni-foam is only 321 mV and 49 mV dec^{-1}, which is much lower than that of IrO_2, indicating the superior OER catalytic activity of Fe_3C. Moreover, compared with wdC-MS, it can also be seen that the peak position in N-wdC-MS shifts to the right, meaning that there may be a strong interaction between N-doped C and Fe_3C caused by the electron transfer [63–66].

3.2. Electrochemical testing

The LSV tests were applied to evaluate the ORR/OER catalytic activity of the as-prepared cathodes and commercial Pt/C (20 *wt.* %) and RuO_2 catalysts in 1 M KOH solution. Fig. 5a & b display the ORR/OER polarization curves of the as-synthesized samples, where the performance of wdC obtained by direct calcination of pure wood is the worst.

After N-doping or molten salt modification, the performance can be improved, and after the joint implementation of these two modification measures, the ORR/OER activity reaches the best value. Clearly, N-wdC-MS exhibits the highest initial potential (0.96 V), highest half-wave potentials ($E_{1/2}$ =0.793 V) and the largest limiting current density (Fig. 5a), which is almost comparable to commercial Pt/C. Although the OER performance of N-wdC-MS is unsatisfactory compared with the commercial IrO_2 catalyst, a low overpotential of 1.75 V (vs. RHE) at 10 mA cm^{-2} highlights its advantages among these four cathodes (Fig. 5b). These results implied that N-wdC-MS could accelerate the kinetics of the generation and decomposing of discharge products by during the battery cycle process [67].

Notably, in most published works, the electrochemical performance test of ORR/OER bifunctional catalysts for Li-O_2 batteries is carried out in aqueous solution. However, the solubility and diffusion rate of O_2 in organic electrolyte are different from that in aqueous solution. In addition, the reaction products in these two electrolyte systems are also
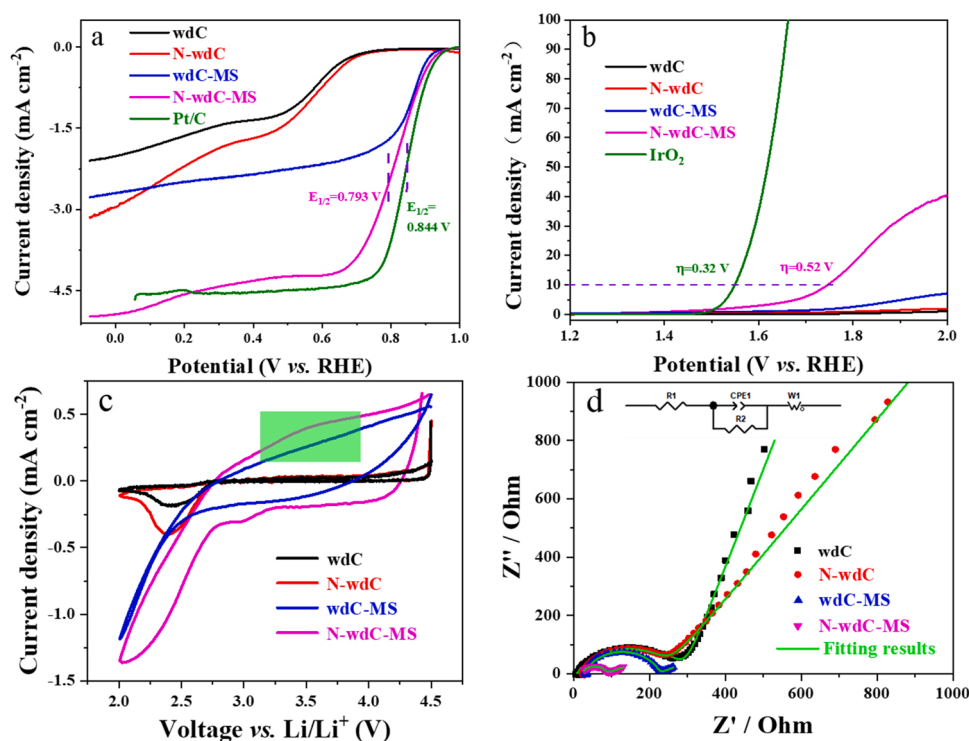
Fig. 5. ORR (a) and OER (b) polarization curves of wdC, N-wdC, wdC-MS and N-wdC-MS in 0.1 M KOH solution; *In-situ* CV curves (c) and EIS (d) of Li-O$_2$ batteries with different cathodes.
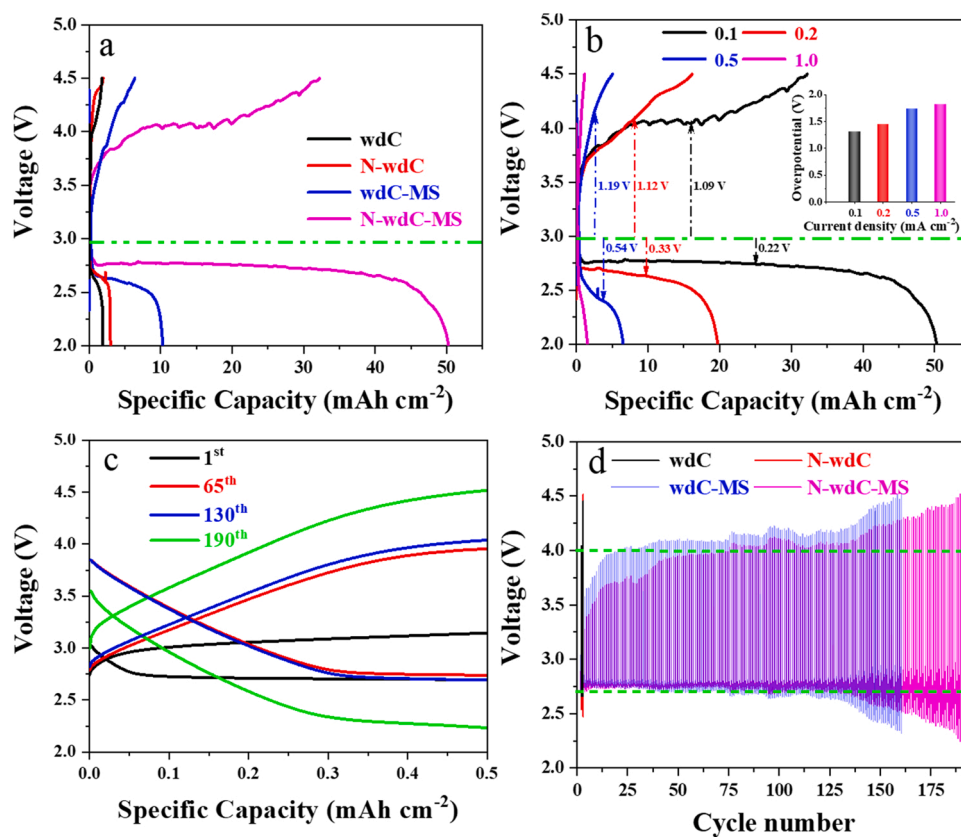

Fig. 6. (a) Discharge/charge curves of Li-O$_2$ batteries with different cathodes at 0.1 mA cm^{-2}. (b) Rate performance of Li-O$_2$ battery with N-wdC-MS. (c) Discharge/charge curves of Li-O$_2$ battery with N-wdC-MS at 0.1 mA cm^{-2} with a limited capacity of 0.5 mAh cm^{-2}. (d) The termination voltages of discharge and charge as a function of cycle numbers.

different. Therefore, in-situ CV tests are necessary (Fig. 5c). In the ORR process, N-wdC-MS showed an onset potential (2.82 V), which is much higher than in other cathodes. In addition, N-wdC-MS also has greater limiting current density. For OER, N-wdC-MS showed a broad oxidation peak at 3.5 V (see the green mark in Fig. 5c), while other electrode materials did not show an obvious oxidation peak. It is suggested that N-wdC-MS may have lower overpotential compared with other cathodes [68].

Fig. 5d shows in-situ EIS spectra of the as synthesized cathodes. All curves show a similar semicircle in the high and medium frequency regions, and an oblique line in the low frequency region. In the equivalent circuit, R_Ω represents the ohmic impedance, R_{ct} and CPE represent charge transfer resistance and electric double-layer capacitance, and W is the impedance of Li^+ ions diffusion. Obviously, as listed in Table S2, N-wdC-MS has a smallest charge transfer resistance, meaning the best catalytic activity. The EIS spectra of the $Li-O_2$ batteries with different cathodes at different stages are shown in Fig. S5 and the corresponding fitting data are listed in Table S3. Clearly, the R_Ω and R_{ct} values increased significantly after discharging, which is undoubtedly attributed to the discharge products covering on the cathode. After charged to 4.5 V, the R_{ct} value of N-wdC-MS is still the smallest and close to that of the pristine cathode, proving the higher catalytic activity of N-wdC-MS.

3.3. Battery performance

The performance of $Li-O_2$ battery with different cathodes are shown in Fig. 6. From Fig. 6a, it is obvious that the specific discharge capacity of wdC is only 1.9 mAh cm^{-2} at 0.1 mA cm^{-2}. By contrast, N-wdC and wdC-MS delivers the specific capacity of 2.98 and 10.3 mAh cm^{-2}. Clearly, the N-doping and the formation of Fe_3C can improve the performance of the battery.

After simultaneous introducing melamine and $FeCl_3/LiCl$, N-wdC-MS shows a striking performance. The specific capacity of N-wdC-MS cathode is 50.4 mAh cm^{-2}, which is the highest value based on non-noble metal cathode reported so far. In addition, the $Li-O_2$ battery with N-wdC-MS delivered a high discharge voltage platform (2.75 V), and the charging voltage platform was slightly higher than 4.0 V.

As can be seen from Fig. 6b, the discharge specific capacity of N-wdC-MS gradually decreases with increasing the current density, which are 19.7 and 6.5 mAh cm^{-2} at 0.2 and 0.5 mA cm^{-2} respectively. Even at 1.0 mA cm^{-2}, the specific capacity of N-wdC-MS can deliver 2.0 mAh cm^{-2}.

In addition, with the current density increasing (0.1, 0.2, 0.5, 1.0 mA cm^{-2}), the mid-capacity overpotentials increases from 1.31 V to 1.44 V, 1.73 V and 1.78 V, respectively (inset of Fig. 6b). The small growth of overpotentials also implies the good rate performance of N-wdC-MS [21]. Table S3 lists the discharge/charge data of $Li-O_2$ batteries with similar cathodes. It can be found that the performance of N-wdC-MS is extremely excellent.

To further test the stability, the $Li-O_2$ battery equipped with various cathodes was performed with the limited capacity mode (0.5 mAh cm^{-2}) at 0.1 mA cm^{-2}, as indicated in Fig. 6c & d. It is obvious that N-wdC-MS cathode can maintain 190 stable cycles, which is significantly better than wdC (1 cycle), N-wdC (2 cycles) and wdC-MS (162 cycles). Besides, the battery with N-wdC-MS produces a discharge voltage of as high as 2.71 V and the charging cut-off voltage of as low as 3.96 V before 75th cycle, with a voltage gap of 1.25 V. By 130th cycle, the N-wdC-MS cathode exhibited a convincing performance with the voltage gap slightly increases to 1.33 V. In the same case, the voltage gap of wdC-MS extends from 1.4 V to 1.53 V, demonstrating the better reversibility of N-wdC-MS.

In order to explore the formation and decomposition of the discharge products, the N-wdC-MS cathode after discharged and charged was took out and analyzed the morphology and material composition of the charge and discharge products by SEM and XRD, as shown in Fig. 7.

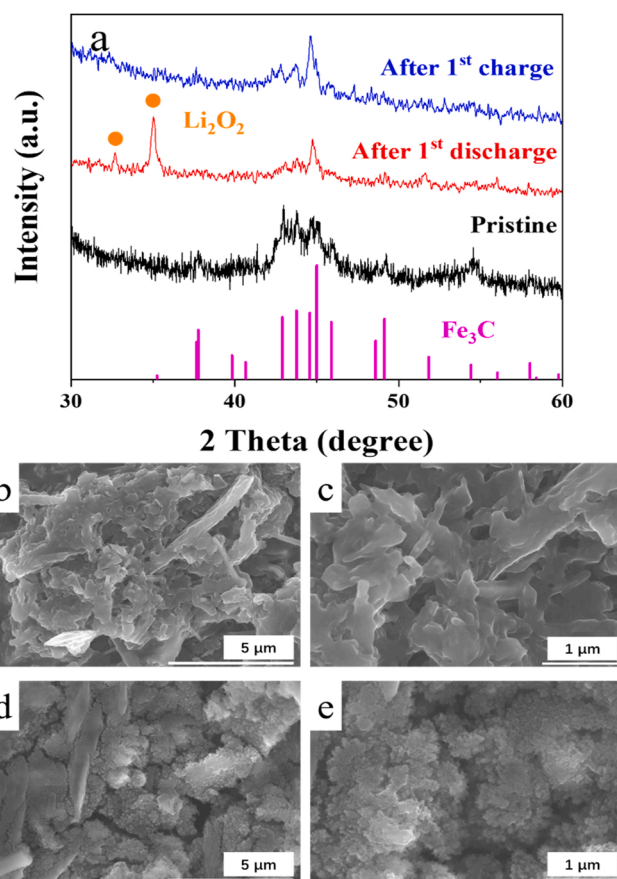It can be seen from the XRD pattern (Fig. 7a) that there is an obvious

Fig. 7. (a) XRD patterns at different stages and (b, c) SEM images of N-wdC-MS after 1st discharged and (d, e) 1st charged.

diffraction peak at 32.5°, corresponding to Li_2O_2 (JCPDF: 09–0355), demonstrating that the discharge product is Li_2O_2 [69,70]. After the recharge, the signal of Li_2O_2 disappears, implying the complete decomposition of Li_2O_2. SEM micrographs show that the surface of N-wdC-MS was covered by film-like with lamellar inclusion Li_2O_2 after discharged to 2.0 V (Fig. 7b & c).

Ma et al. [71] investigated the morphology of Li_2O_2 on different F-doped cathode and found that different F doping amounts correspond to different appearance of Li_2O_2. Film-like Li_2O_2 with granular inclusion was uniformly dispersed on the surface of 100 FC, while nanorod and toroid-like Li_2O_2 was formed on the surface of 0 FC and 200 FC respectively. The authors suggested that the formation of film-like Li_2O_2 can increase the contact area with the cathode, enhance the electron transfer ability and facilitate the decomposition of Li_2O_2. After charging to 4.5 V, the original morphology of the electrode surface is re-exposed (Fig. 7d & e), confirming the excellent OER activity of N-wdC-MS.

4. Conclusions

In this paper, a 3D self-supporting carbonized wood electrode was prepared by high temperature pyrolysis with $FeCl_3/LiCl$ impregnated paulownia wood and melamine, which was directly used as the cathode of $Li-O_2$ battery. The introduction of $FeCl_3/LiCl$ can introduce a higher porous structure into carbonized wood and increase the specific surface area and mesoporous ratio, resulting in the increase of the electrochemical three-phase reaction interface. The melamine introduces heteroatoms into carbonized wood, which improves the defect degree of electrode material, conducing to enhance the electrochemical activity. The vertical channel structure inherited from wood is beneficial for the accelerated mass transfer at the electrode. This simple method opens a

new field of vision for the synthesis of low-cost and high-performance Li-O_2 battery cathode.

Credit authorship contribution statement

Huagen Liang: Conceptualization, Methodology, Investigation, Writing – original draft. **Zejia Gai**: Validation, Formal analysis, Writing – original draft. **Fu Chen**: Methodology, Writing – original draft, Formal analysis. **Shengyu Jing**: Conceptualization, Writing – review & editing, Funding acquisition. **Wei Kan**: Conceptualization, Validation, Formal analysis. **Bing Zhao**: Investigation, Methodology, Validation. **Shibin Yin**: Validation, Writing – review & editing. **Panagiotis Tsiakaras**: Conceptualization, Validation, Writing – review & editing.

Declaration of Competing Interest

The authors declare that they have no known competing financial interests or personal relationships that could have appeared to influence the work reported in this paper.

Data Availability

Data will be made available on request.

Appendix A. Supporting information

Supplementary data associated with this article can be found in the online version at doi:10.1016/j.apcatb.2022.122203.

References

[1] D. Cao, Y. Chen, Ultimate Li-ion batteries, Sci. Bull. 66 (2021) 645–647, https://doi.org/10.1016/j.scib.2020.11.011.
[2] T. Liu, J.P. Vivek, E.W. Zhao, J. Lei, N. Garcia-Araez, C.P. Grey, Current challenges and routes forward for nonaqueous lithium-air batteries, Chem. Rev. 120 (2020) 6558–6625, https://doi.org/10.1021/acs.chemrev.9b00545.
[3] W.-J. Kwak, Rosy, D. Sharon, C. Xia, H. Kim, L.R. Johnson, P.G. Bruce, L.F. Nazar, Y.-K. Sun, A.A. Frimer, M. Noked, S.A. Freunberger, D. Aurbach, Lithium-oxygen batteries and related systems: potential, status, and future, ACS Cent. Sci. 120 (2020) 6626–6683, https://doi.org/10.1021/acs.chemrev.9b00609.
[4] H. Wang, F.X. Yin, N. Liu, R.H. Kou, X.B. He, C.J. Sun, B.H. Chen, D.J. Liu, H. Q. Yin, Engineering Fe-Fe$_3$C@Fe-N-C active sites and hybrid structures from dual metal-organic frameworks for oxygen reduction reaction in H$_2$-O$_2$ fuel cell and Li-O$_2$ battery, Adv. Funct. Mater. 29 (2019), 1901531, https://doi.org/10.1002/adfm.201901531.
[5] J.W. Jung, S.H. Cho, J.S. Nam, I.D. Kim, Current and future cathode materials for non-aqueous Li-air (O$_2$) battery technology – a focused review, Energy Stor. Mater. 24 (2019) 512–528, https://doi.org/10.1016/j.ensm.2019.07.006.
[6] C. Tan, D. Cao, L. Zheng, Y. Shen, L. Chen, Y. Chen, True reaction sites on discharge in Li-O$_2$ batteries, J. Am. Chem. Soc. 144 (2022) 807–815, https://doi.org/10.1021/jacs.1c09916.
[7] J. Wang, L. Ma, J. Xu, Y. Xu, K. Sun, Z. Peng, Oxygen electrochemistry in Li-O$_2$ batteries probed by in situ surface-enhanced Raman spectroscopy, SusMat 1 (2021) 345–358, https://doi.org/10.1002/sus2.24.
[8] P. Zhang, M.J. Ding, X.X. Li, C.X. Li, Z.Q. Li, L.W. Yin, Challenges and strategy on parasitic reaction for high-performance nonaqueous lithium-oxygen batteries, Adv. Eng. Mater. 10 (2020) 2001789, https://doi.org/10.1002/aenm.202001789.
[9] M. Balaish, J.W. Jung, I.D. Kim, Y.E. Eli, A critical review on functionalization of air-cathodes for nonaqueous Li-O$_2$ batteries, Adv. Funct. Mater. 30 (2019), 1808303, https://doi.org/10.1002/adfm.201808303.
[10] X. Peng, C. Wang, Y. Liu, W. Fang, Y. Zhu, L. Fu, J. Ye, L. Liu, Y. Wu, Critical advances in re-engineering the cathode-electrolyte interface in alkali metal-oxygen batteries, Energy Mater. 1 (2021), 100011, https://doi.org/10.20517/energymater.2021.15.

[11] Y.J. Wang, B.Z. Fang, D. Zhang, A.J. Li, D.P. Wilkinson, A. Ignaszak, L. Zhang, J. J. Zhang, A review of carbon-composited materials as air-electrode bifunctional electrocatalysts for metal-air batteries, Electrochem. Energy Rev. 1 (2018) 1–34, https://doi.org/10.1007/s41918-018-0002-3.
[12] L. Ma, T. Yu, E. Tzoganakis, K. Amine, T. Wu, Z. Chen, J. Lu, Fundamental understanding and material challenges in rechargeable nonaqueous Li-O$_2$ batteries: recent progress and perspective, Adv. Eng. Mater. 8 (2018), 1800348, https://doi.org/10.1002/aenm.201800348.
[13] H. Liang, Y. Zhang, F. Chen, S. Jing, S. Yin, P. Tsiakaras, A novel NiFe@NC-functionalized N-doped carbon microtubule network derived from biomass as a highly efficient 3D free-standing cathode for Li-CO$_2$ batteries, Appl. Catal. B 244 (2019) 559–567, https://doi.org/10.1016/j.apcatb.2018.11.075.
[14] S. Wei, C. Wan, Y. Jiao, X. Li, J. Li, Y. Wu, 3D nanoflower-like MoSe$_2$ encapsulated with hierarchically anisotropic carbon architecture: a new and free-standing anode with ultra-high areal capacitance for asymmetric supercapacitors, ChemComm 56 (2020) 340–343, https://doi.org/10.1039/c9cc07362k.
[15] H. Qin, Y. Zhou, Q. Huang, Z. Yang, R. Dong, L. Li, J. Tang, C. Zhang, F. Jiang, Metal Organic Framework (MOF)/wood derived multi-cylinders high-power 3D reactor, ACS Appl. Mater. Interfaces 13 (2021) 5460–5468, https://doi.org/10.1021/acsami.0c21664.
[16] S. Min, W. Deng, Y. Li, F. Wang, Z. Zhang, Self-supported CoP nanoparticle-embedded wood-derived porous carbon membrane for efficient H$_2$ evolution in both acidic and basic solutions, ChemCatChem 12 (2020) 3929, https://doi.org/10.1002/cctc.202000407.
[17] W. Zhang, Y. Yang, R. Xia, Y. Li, J. Zhao, L. Lin, J. Cao, Q. Wang, Y. Liu, H. Guo, Graphene-quantum-dots-induced MnO$_2$ with needle-like nanostructure grown on carbonized wood as advanced electrode for supercapacitors, Carbon 162 (2020) 114–123, https://doi.org/10.1016/j.carbon.2020.02.039.
[18] L. Li, R. Xiao, X. Tao, X. Wu, L. Jiang, Z. Zhang, Y. Qing, Free-standing electrodes via coupling nanostructured Ni-NiO with hierarchical wood carbon for high-performance supercapacitors and Ni-Zn batteries, J. Power Sources 491 (2021), 229618, https://doi.org/10.1016/j.jpowsour.2021.229618.
[19] Y. Zheng, Y. Song, T. Gao, S. Yan, H. Hu, F. Cao, Y. Duan, X. Zhang, Lightweight and hydrophobic three-dimensional wood-derived anisotropic magnetic porous carbon for highly efficient electromagnetic interference shielding, ACS Appl. Mater. Interfaces 12 (2020) 40802–40814, https://doi.org/10.1021/acsami.0c11530.
[20] Q. Zhang, L. Li, B. Jiang, H. Zhang, N. He, S. Yang, D. Tang, Y. Song, Flexible and mildew-resistant wood-derived aerogel for stable and efficient solar desalination, ACS Appl. Mater. Interfaces 12 (2020) 28179–28187, https://doi.org/10.1021/acsami.0c05806.
[21] H. Song, S. Xu, Y. Li, J. Dai, A. Gong, M. Zhu, C. Zhu, C. Chen, Y. Chen, Y. Yao, B. Liu, J. Song, G. Pastel, L. Hu, Hierarchically porous, ultrathick, "Breathable" wood-derived cathode for lithium-oxygen batteries, Adv. Eng. Mater. 8 (2018), 1701203, https://doi.org/10.1002/aenm.201701203.
[22] Y. Qiao, S. Xu, Y. Liu, J. Dai, H. Xie, Y. Yao, X. Mu, C. Chen, D.J. Kline, E. Hitz, B. Liu, J. Song, P. He, M. Zachariah, L. Hu, Transient, in situ synthesis of ultrafine ruthenium nanoparticles for a high-rate Li-CO$_2$ battery, Energy Environ. Sci. 12 (2019) 1100, https://doi.org/10.1039/c8ee03506g.
[23] S. Xu, C. Chen, Y. Kuang, J. Song, W. Gan, B. Liu, E.M. Hitz, J.W. Connell, Y. Lin, L. Hu, Flexible lithium-CO$_2$ battery with ultrahigh capacity and stable cycling, Energy Environ. Sci. 11 (2018) 3231–3237, https://doi.org/10.1039/c8ee01468j.
[24] C. Zhu, L. Du, J. Luo, H. Tang, Z. Cui, H. Song, S. Liao, A renewable wood-derived cathode for Li-O$_2$ batteries, J. Mater. Chem. A 6 (2018) 14291–14298, https://doi.org/10.1039/c8ta04703k.
[25] C. Chen, S. Xu, Y. Kuang, W. Gan, J. Song, G. Chen, G. Pastel, B. Liu, Y. Li, H. Huang, L. Hu, Nature-Inspired tri-pathway design enabling high-performance flexible Li-O$_2$ batteries, Adv. Eng. Mater. 9 (2019), 1802964, https://doi.org/10.1002/aenm.201802964.
[26] J. Luo, X. Yao, L. Yang, Y. Han, L. Chen, X. Geng, V. Vattipalli, Q. Dong, W. Fan, D. Wang, H. Zhu, Free-standing porous carbon electrodes derived from wood for high-performance Li-O$_2$ battery applications, Nano Res. 10 (2017) 4318–4326, https://doi.org/10.1007/s12274-017-1660-x.
[27] Z. Tang, Z. Pei, Z. Wang, H. Li, J. Zeng, Z. Ruan, Y. Huang, M. Zhu, Q. Xue, J. Yu, C. Zhi, Highly anisotropic, multichannel wood carbon with optimized heteroatom doping for supercapacitor and oxygen reduction reaction, Carbon 130 (2018) 532–543, https://doi.org/10.1016/j.carbon.2018.01.055.
[28] X. Peng, L. Zhang, Z. Chen, L. Zhong, D. Zhao, X. Chi, X. Zhao, L. Li, X. Lu, K. Leng, C. Liu, W. Liu, W. Tang, K.P. Loh, Hierarchically porous carbon plates derived from wood as bifunctional ORR/OER electrodes, Adv. Mater. 31 (2019), 1900341, https://doi.org/10.1002/adma.201900341.
[29] Z. Yang, H. Nie, Xa Chen, X. Chen, S. Huang, Recent progress in doped carbon nanomaterials as effective cathode catalysts for fuel cell oxygen reduction reaction, J. Power Sources 236 (2013) 238–249, https://doi.org/10.1016/j.jpowsour.2013.02.057.
[30] X. Chen, P. Cheng, Z. Tang, X. Xu, H. Gao, G. Wang, Carbon-based composite phase change materials for thermal energy storage, transfer, and conversion, Adv. Sci. 8 (2021) 2001274, https://doi.org/10.1002/advs.202001274.
[31] H. Pang, P. Sun, H. Gong, N. Zhang, J. Cao, R. Zhang, M. Luo, Y. Li, G. Sun, Y. Li, J. Deng, M. Gao, M. Wang, B. Kong, Wood-derived bimetallic and heteroatomic hierarchically porous carbon aerogel for rechargeable flow Zn-Air batteries, ACS Appl. Mater. Interfaces 13 (2021) 39458–39469, https://doi.org/10.1021/acsami.1c10925.
[32] X. Cui, Y. Liu, G. Han, M. Cao, L. Han, B. Zhou, S. Mehdi, X. Wu, B. Li, J. Jiang, Wood-derived integral air electrode for enhanced interfacial electrocatalysis in

rechargeable zinc-air battery, Small 17 (2021), 2101607, https://doi.org/10.1002/smll.202101607.

[33] Y. Chen, S. Ji, H. Wang, V. Linkov, R. Wang, Synthesis of porous nitrogen and sulfur co-doped carbon beehive in a high-melting-point molten salt medium for improved catalytic activity toward oxygen reduction reaction, Int. J. Hydrog. Energy 43 (2018) 5124–5132, https://doi.org/10.1016/j.ijhydene.2018.01.095.

[34] N. Díez, A.B. Fuertes, M. Sevilla, Molten salt strategies towards carbon materials for energy storage and conversion, Energy Stor. Mater. 38 (2021) 50–69, https://doi.org/10.1016/j.ensm.2021.02.048.

[35] K. Xiao, L.-X. Ding, G. Liu, H. Chen, S. Wang, H. Wang, Freestanding, hydrophilic nitrogen-doped carbon foams for highly compressible all solid-state supercapacitors, Adv. Mater. 28 (2016) 5997–6002, https://doi.org/10.1002/adma.201601125.

[36] S. Lee, G. Kim, J. Kim, D. Kim, D. Lee, H. Han, J. Kim, Nitrogen-Doped porous carbon structure from melamine-assisted polyimide sheets for supercapacitor electrodes, Adv. Sustain. Syst. 2 (2018), 1800007, https://doi.org/10.1002/adsu.201800007.

[37] Y. Lai, W. Chen, Z. Zhang, Y. Qu, Y. Gan, J. Li, Fe/Fe$_3$C decorated 3-D porous nitrogen-doped graphene as a cathode material for rechargeable Li-O$_2$ batteries, Electrochim. Acta 191 (2016) 733–742, https://doi.org/10.1016/j.electacta.2016.01.134.

[38] G. Zhang, X. Liu, L. Wang, F. Sun, Y. Yang, C. Tian, P. Yu, Q. Pan, H. Fu, B. N-Doped, Defective carbon entangled Fe$_3$C nanoparticles as the superior oxygen reduction electrocatalyst for Zn-Air batteries, ACS Sustain. Chem. Eng. 7 (2019) 19104–19112, https://doi.org/10.1021/acssuschemeng.9b05033.

[39] T.Y. Burshtein, D. Aias, J. Wang, M. Sananis, E.M. Farber, O.M. Gazit, I. Grinberg, D. Eisenberg, Fe-N-C electrocatalysts in the oxygen and nitrogen cycles in alkaline media: the role of iron carbide, Phys. Chem. Chem. Phys. 23 (2021) 26674–26679, https://doi.org/10.1039/D1CP03650E.

[40] Y. Zhang, L.-B. Huang, W.-J. Jiang, X. Zhang, Y.-Y. Chen, Z. Wei, L.-J. Wan, J.-S. Hu, Sodium chloride-assisted green synthesis of a 3D Fe-N-C hybrid as a highly active electrocatalyst for the oxygen reduction reaction, J. Mater. Chem. A 4 (2016) 7781–7787, https://doi.org/10.1039/C6TA01655C.

[41] X. Liu, C. Giordano, M. Antonietti, A facile molten-salt route to graphene synthesis, Small 10 (2014) 193–200, https://doi.org/10.1002/smll.201300812.

[42] X. Liu, N. Fechler, M. Antonietti, Salt melt synthesis of ceramics, semiconductors and carbon nanostructures, Chem. Soc. Rev. 42 (2013) 8237–8265, https://doi.org/10.1039/C3CS60159E.

[43] Q. Dong, H. Wang, S. Ji, X. Wang, Z. Mo, V. Linkov, R. Wang, Molten-salt media synthesis of N-Doped carbon tubes containing encapsulated Co nanoparticles as a bifunctional air cathode for zinc-air batteries, Chem. -A Eur. J. 26 (2020) 10752–10758, https://doi.org/10.1002/chem.201905268.

[44] Z. Pang, G. Li, X. Xiong, L. Ji, Q. Xu, X. Zou, X. Lu, Molten salt synthesis of porous carbon and its application in supercapacitors: a review, J. Energy Chem. 61 (2021) 622–640, https://doi.org/10.1016/j.jechem.2021.02.020.

[45] C. Wang, D. Wu, H. Wang, Z. Gao, F. Xu, K. Jiang, A green and scalable route to yield porous carbon sheets from biomass for supercapacitors with high capacity, J. Mater. Chem. A 6 (2018) 1244–1254, https://doi.org/10.1039/C7TA07579K.

[46] W. Zhao, P.H. Tan, J. Liu, A.C. Ferrari, Intercalation of few-layer graphite flakes with FeCl$_3$: raman determination of fermi level, layer by layer decoupling, and stability, J. Am. Chem. Soc. 133 (2011) 5941–5946, https://doi.org/10.1021/ja110939a.

[47] Z. Li, H. He, H. Cao, S. Sun, W. Diao, D. Gao, P. Lu, S. Zhang, Z. Guo, M. Li, R. Liu, D. Ren, C. Liu, Y. Zhang, Z. Yang, J. Jiang, G. Zhang, Atomic Co/Ni dual sites and Co/Ni alloy nanoparticles in N-doped porous Janus-like carbon frameworks for bifunctional oxygen electrocatalysis, Appl. Catal. B 240 (2019) 112–121, https://doi.org/10.1016/j.apcatb.2018.08.074.

[48] Y. Yang, X. Sun, Z. Cheng, A. Mukhopadhyay, A. Natan, C. Liu, D. Cao, H. Zhu, Functionalized well-aligned channels derived from wood as a convection-enhanced electrode for aqueous flow batteries, Appl. Energy Mater. 3 (2020) 6249–6257, https://doi.org/10.1021/acsaem.0c00354.

[49] X. Tao, H. Xu, S. Luo, Y. Wu, C. Tian, X. Lu, Y. Qing, Construction of N-doped carbon nanotube encapsulated active nanoparticles in hierarchically porous carbonized wood frameworks to boost the oxygen evolution reaction, Appl. Catal. B 279 (2020), 119367, https://doi.org/10.1016/j.apcatb.2020.119367.

[50] X. Cui, L. Gao, S. Lei, S. Liang, J. Zhang, C.D. Sewell, W. Xue, Q. Liu, Z. Lin, Y. Yang, Simultaneously crafting single-atomic Fe sites and graphitic layer-wrapped Fe$_3$C nanoparticles encapsulated within mesoporous carbon tubes for oxygen reduction, Adv. Funct. Mater. 31 (2020), 2009197, https://doi.org/10.1002/adfm.202009197.

[51] Z. Liu, Y. Zhu, K. Xiao, Y. Xu, Y. Peng, J. Liu, X. Chen, Fe/Fe$_3$C embedded in N-Doped worm-like porous carbon for highrate catalysis in rechargeable zinc-air batteries, ACS Appl. Mater. Interfaces 13 (2021) 24710–24722, https://doi.org/10.1021/acsami.1c03220.

[52] H. Yu, D. Zhang, Z. Fang, S. Xu, Q. Liu, H. Hou, L. Wang, Z. Zhou, G. Shao, W. Yang, J. Teng, S. Chen, N and S Co-doped carbon nanofibers with embedded candle soot and designed surface decoration for efficient bifunctional

electrocatalysts, Electrochim. Acta 380 (2021), 138261, https://doi.org/10.1016/j.electacta.2021.138261.

[53] G. Daniel, M. Mazzucato, R. Brandiele, L.D. Lazzari, D. Badocco, P. Pastore, T. Kosmala, G. Granozzi, C. Durante, Sulfur doping versus hierarchical pore structure: the dominating effect on the Fe-N-C site density, activity, and selectivity in oxygen reduction electrocatalysis, ACS Appl. Mater. Interfaces 13 (2021) 42693–42705, https://doi.org/10.1021/acsami.1c09659.

[54] W. Weng, J. Zhou, D. Gu, W. Xiao, Thermoelectrochemical formation of Fe/Fe$_3$C@ hollow N-doped carbon in molten salts for enhanced catalysis, J. Mater. Chem. A 8 (2020) y–4806, https://doi.org/10.1039/d0ta00565g.

[55] J. Gao, S. Liu, P. Zhou, X. Zhao, G. Wang, Fe-N$_4$ engineering of S and N co-doped hierarchical porous carbon-based electrocatalysts for enhanced oxygen reduction in Zn-air batteries, Dalton Trans. 49 (2020) y–14853, https://doi.org/10.1039/d0dt02704a.

[56] Y. Peng, P. Wang, J. Yang, S. Lu, K. Li, G. Liu, Y. Duan, J. Qiu, Decorating ZIF-67-derived cobalt-nitrogen doped carbon nanocapsules on 3D carbon frameworks for efficient oxygen reduction and oxygen evolution, Carbon 177 (2021) 344–356, https://doi.org/10.1016/j.carbon.2021.02.052.

[57] A.A. Eissa, N.H. Kim, J.H. Lee, Rational design of highly mesoporous Fe-N-C/Fe$_3$C/C-S-C nanohybride with dense active sites for superb electrocatalysis of oxygen reduction, J. Mater. Chem. A 8 (2020) y–23454, https://doi.org/10.1039/d0ta06987f.

[58] M. Peng, Y. Qiao, M. Luo, M. Wang, S. Chu, Y. Zhao, P. Liu, J. Liu, Y. Tan, Bioinspired Fe$_3$C@C as highly efficient electrocatalyst for nitrogen reduction reaction under ambient conditions, ACS Appl. Mater. Interfaces 11 (2019) 40062–40068, https://doi.org/10.1021/acsami.9b14143.

[59] Y. Zhao, J. Zhang, X. Guo, H. Fan, W. Wu, H. Liu, G. Wang, Fe$_3$C@Nitrogen doped CNTs arrays aligned on nitrogen functionalized carbon nanofibers as highly efficient catalysts for oxygen evolution reaction, J. Mater. Chem. A 5 (2017) y–19679, https://doi.org/10.1039/C7TA05936A.

[60] C.C. Yang, S.F. Zai, Y.T. Zhou, L. Du, Q. Jiang, Fe$_3$C-Co nanoparticles encapsulated in a hierarchical structure of N-Doped carbon as a multifunctional electrocatalyst for ORR, OER, and HER, Adv. Funct. Mater. 29 (2019), https://doi.org/10.1002/adfm.201901949.

[61] X. Fan, Z. Peng, R. Ye, H. Zhou, X. Guo, M$_3$C (M: Fe, Co, Ni) nanocrystals encased in graphene nanoribbons: an active and stable bifunctional electrocatalyst for oxygen reduction and hydrogen evolution reactions, ACS Nano 9 (2015) y–7418, https://doi.org/10.1021/acsnano.5b02420.

[62] S. Zhu, J. Lei, L. Zhang, L. Lu, Efficient electrocatalytic oxygen evolution by Fe$_3$C nanosheets perpendicularly grown on 3D Ni foams, Int. J. Hydrog. Energy 44 (2019) 16507–16515, https://doi.org/10.1016/j.ijhydene.2019.04.214.

[63] Y.-H. Zhao, T. Zhang, X. Wang, S. Li, Y. Pan, Y. Wang, X. Song, Z. Tan, Plant polyphenols involved coordination assemblies derived Mo$_3$Co$_3$C/Mo$_2$C/Co@NC with phase regulation and interface engineering for efficient hydrogen evolution reaction electrocatalysis, N. J. Chem. 46 (2022) 13030y–13036, https://doi.org/10.1039/d2nj01810a.

[64] H. Zhao, S. Yang, W. Yang, C. Zhao, M. Cao, R. Cao, Ultrasmall Mo$_2$C embedded in N-doped holey carbon derived from macrocycle supramolecular self-assembly for high-efficiency electrochemical oxygen reduction reaction, ChemElectroChem 9 (2022) y, https://doi.org/10.1002/celc.202200141.

[65] X. Zhang, Y.-A. Li, Y. Huang, H. Mu, X. Gu, F. Li, Z. Wang, J. Li, Impacts of metal-support interaction on hydrogen evolution reaction of cobalt-nitride-carbide catalyst, Front. Chem. 9 (2022), 828964, https://doi.org/10.3389/fchem.2021.828964.

[66] H. Ma, Z. Chen, Z. Wang, C.V. Singh, Q. Jiang, Interface engineering ofCo/CoMoN/NF heterostructures for high-performance electrochemical overall water splitting, Adv. Sci. 9 (2022), 2105313, https://doi.org/10.1002/advs.202105313.

[67] Y. Zhan, S.-z Yu, S.-h Luo, J. Feng, Q. Wang, Nitrogen-Coordinated CoS$_2$@NC yolk−shell polyhedrons catalysts derived from a metal-organic framework for a highly reversible Li-O$_2$ battery, ACS Appl. Mater. Interfaces 13 (2021) 17658–17667, https://doi.org/10.1021/acsami.1c02564.

[68] Z. Yin, Y.D. Feng, G.Q. Feng, Z.S. Hua, W. Li, P.H. Gen, Z. Yong, Implanting cation vacancies in Ni-Fe LDHs for efficient oxygen evolution reactions of lithium-oxygen batteries, Appl. Catal. B 285 (2021) y, https://doi.org/10.1016/j.apcatb.2020.119792.

[69] F. Xiao, Z. Lin, J. Zhang, Y. Lei, Y. Meng, X. Chen, S. Zhao, B. Hong, J. Wang, D. Li, J. Xu, A. Novel, Approach to facile synthesis of boron and nitrogen co-doped carbon and its application in lithium oxygen batteries, energy stor, Energy Stor. Mater. 41 (2021) y–68, https://doi.org/10.1016/j.ensm.2021.05.042.

[70] H. Biao, L.G. Yang, L.J. Jia, W. Jun, T. Hui, F.Y. Qi, W.W. Liang, S.S. Hui, D. Feng, MoSe$_2$@CNT core-shell nanostructures as grain promoters featuring a direct Li$_2$O$_2$ formation/decomposition catalytic capability in lithium-oxygen batteries, Adv. Eng. Mater. 11 (2021) 2003263, https://doi.org/10.1002/aenm.202003263.

[71] S. Ma, H. Yao, Z. Li, Q. Liu, Tuning the nucleation and decomposition of Li$_2$O$_2$ by fluorine-doped carbon vesicles towards high performance Li-O$_2$ batteries, J. Energy Chem. 70 (2022) 614y–622, https://doi.org/10.1016/j.jechem.2022.03.007.